

## Article

# Phosphoprotein Detection in Sweat Realized by Intercalation Structure 2D@3D g-C<sub>3</sub>N<sub>4</sub>@Fe<sub>3</sub>O<sub>4</sub> Wearable Sensitive Motif

Yuting Qiao <sup>1,†</sup>, Lijuan Qiao <sup>2,\*,†</sup>, Peize Zhao <sup>1</sup>, Peng Zhang <sup>1</sup> , Fanbin Wu <sup>1</sup>, Jiahui Zhang <sup>1</sup>, Li Gao <sup>1,\*</sup>, Bingxin Liu <sup>1,\*</sup>  and Lei Zhang <sup>3</sup>

<sup>1</sup> School of Mechanical Engineering, Qinghai University, Xining 810016, China; hiyutingqqq@126.com (Y.Q.); 18733006311@163.com (P.Z.); zhangpeng@qhu.edu.cn (P.Z.); wfb632292561@126.com (F.W.); z276475670@126.com (J.Z.)

<sup>2</sup> Research Center of Basic Medical Science, Medical College, Qinghai University, Xining 810016, China

<sup>3</sup> Department of Mechanical Engineering, University of Alaska Fairbanks, P.O. Box 755905, Fairbanks, AK 99775-5905, USA; lzhang14@alaska.edu

\* Correspondence: 2014980007@qhu.edu.cn (L.Q.); 2007990030@qhu.edu.cn (L.G.); liubx408@nenu.edu.cn (B.L.); Fax: +86-97-1531-0440 (B.L.)

† These authors contributed equally to this work.

**Abstract:** Abnormal protein phosphorylation in sweat metabolites is closely related to cancer, cardiovascular disease, and other diseases. The real-time monitoring of phosphoproteins in sweat is significant for early monitoring of disease biomarkers. Here, a high-efficiency electrochemical sensor for phosphoprotein in sweat was realized by 2D@3D g-C<sub>3</sub>N<sub>4</sub>@Fe<sub>3</sub>O<sub>4</sub> with intercalation structure. Common phosphoprotein β-Casein was selected to demonstrate the platform's functionalities. The detection limit of g-C<sub>3</sub>N<sub>4</sub>@Fe<sub>3</sub>O<sub>4</sub> could be as low as 9.7 μM, and the detection range was from 0.01 mg/mL to 1 mg/mL. In addition, the sensing platform showed good selectivity, reproducibility, and stability. We also investigated the effects of interface structure on adsorption properties and electronic properties of the g-C<sub>3</sub>N<sub>4</sub> and Fe<sub>3</sub>O<sub>4</sub> heterostructure using DFT. More electrons from Fe<sub>3</sub>O<sub>4</sub> were transferred to g-C<sub>3</sub>N<sub>4</sub>, which increased the electrons in the energy band of N atoms and promoted the formation of stable N-H bonds with H atoms in phosphoproteins. We demonstrated phosphoprotein sensor functionality by measuring the phosphoprotein in human sweat during exercising. This work realizes a sensing platform for noninvasive and continuous detection of sweat phosphoproteins in wearable devices.

**Keywords:** g-C<sub>3</sub>N<sub>4</sub>; Fe<sub>3</sub>O<sub>4</sub>; phosphoprotein; sweat sensor



**Citation:** Qiao, Y.; Qiao, L.; Zhao, P.; Zhang, P.; Wu, F.; Zhang, J.; Gao, L.; Liu, B.; Zhang, L. Phosphoprotein Detection in Sweat Realized by Intercalation Structure 2D@3D g-C<sub>3</sub>N<sub>4</sub>@Fe<sub>3</sub>O<sub>4</sub> Wearable Sensitive Motif. *Biosensors* **2022**, *12*, 361. <https://doi.org/10.3390/bios12060361>

Received: 7 May 2022

Accepted: 20 May 2022

Published: 24 May 2022

**Publisher's Note:** MDPI stays neutral with regard to jurisdictional claims in published maps and institutional affiliations.



**Copyright:** © 2022 by the authors. Licensee MDPI, Basel, Switzerland. This article is an open access article distributed under the terms and conditions of the Creative Commons Attribution (CC BY) license (<https://creativecommons.org/licenses/by/4.0/>).

## 1. Introduction

Real-time noninvasive monitoring of various biomarkers in the human body has practical significance for early disease prevention and biomedical diagnosis. In daily medical testing, biological fluids, such as blood and urine, are often used for disease analysis, but it is difficult to achieve the purpose of real-time monitoring [1].

Sweat is also a kind of biological fluid, which includes common substances, such as glucose, urea, electrolytes, and lactic acid [2]. Moreover, the exocrine of human sweat contains a relatively low concentration of protein. It has been reported that the measured concentration range of proteins is about 0.3 mg/mL to 1.12 mg/mL [3], and its abnormal expression can cause diseases, such as atopic dermatitis, schizophrenia, cancer, and tuberculosis [4]. Therefore, the monitoring of protein molecules in sweat helps people to understand whether abnormal translation and expression occur.

Protein phosphorylation is one of the translational modifications in almost all cellular processes, which occurs in serine, threonine, and tyrosine. It plays an important role in physiological processes, such as cell signal transmission, cell growth cycle control, and cell apoptosis [5–7]. About 30% of human protein genome codes contain covalent phosphates

that can be phosphorylated transiently or permanently [8,9]. Abnormal protein phosphorylation may cause Alzheimer's disease [10], schizophrenia [11], Parkinson's disease [12], cancer [13], cardiovascular disease [14], and other diseases. Using phosphorylated proteomics to characterize phosphorylation sites is of great significance to comprehensively understand the markers of disease diagnosis, study the underlying mechanisms, and find relevant treatment strategies.

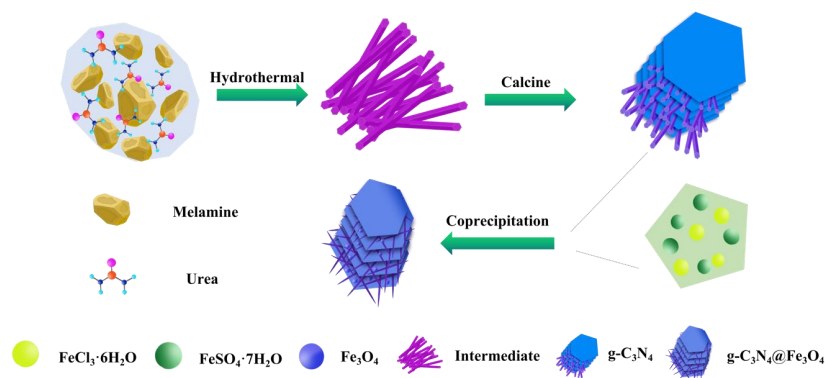
In our work, we identified 109 different types of phosphoproteins and established their associations with different physiological states of the human body through proteomic studies using sweat as a biological sample (Supplementary Materials, Figure S1). At present, many research contributions have been made to the related research on phosphorylated protein in sweat and diseases [15–18]. Therefore, it is still a relatively important opportunity to introduce a method based on the detection of phosphoproteins enrichment in sweat into the wearable electrochemical sensor.

However, it still needs to be considered that, since the protein redox centers usually exist inside three-dimensional protein shells or folded polypeptide shells, the resulting non-specific adsorption and bioincompatibility generally lead to electrode passivation [19,20]. Therefore, the construction of protein electrochemical biosensors still has certain challenges.

In recent years, semiconductor nanomaterials represented by graphitic carbon nitride ( $g\text{-C}_3\text{N}_4$ ) have attracted extensive attention due to their excellent chemical stability, thermal stability, catalytic activity, photoelectric properties, and biocompatibility [21]. The  $g\text{-C}_3\text{N}_4$  is an analog of graphite, mainly composed of p-conjugated graphite [22], in which the covalent atomic layers between carbon and nitrogen are connected to each other by van der Waals forces [23]. However, pure  $g\text{-C}_3\text{N}_4$  has poor conductivity and fewer active sites. Thus, the electronic structure of pure  $g\text{-C}_3\text{N}_4$  framework can be changed by doping with heteroatoms, such as nitrogen, and promote electrochemical performance [24].

The exocrine secretions in human sweat have very low levels of protein and even lower of phosphoproteins. Therefore, a material with specific adsorption capacity for phosphoproteins is required to achieve better enrichment of phosphoproteins in sweat. To date, the technology of functionally modifying magnetic nanomaterials has been verified to be used to efficiently enrich and analyze low-abundance phosphoproteins [25]. Among them,  $\text{Fe}_3\text{O}_4$  nanoparticles, as one of the most important nanostructure materials, can be highly sensitive and selective when combined with phosphate groups, mainly relying on the interaction between the Lewis acid and base [26].

Here, we report a 2D@3D  $g\text{-C}_3\text{N}_4@\text{Fe}_3\text{O}_4$  composite with an intercalation structure for electrochemical detection of phosphoprotein in sweat. The synthesized procedure for the  $g\text{-C}_3\text{N}_4@\text{Fe}_3\text{O}_4$  sensor elements is illustrated in Scheme 1. In addition,  $\beta$ -Casein was used as a model protein to study the coordination mechanism of the structure-activity relationship between phosphoproteins and  $g\text{-C}_3\text{N}_4@\text{Fe}_3\text{O}_4$ . A facile electrochemical strategy for real-time monitoring of phosphoproteins in sweat was developed, which could be further broadly applied in the healthcare field.



**Scheme 1.** Schematic diagram illustrating the  $g\text{-C}_3\text{N}_4@\text{Fe}_3\text{O}_4$  intercalation structure composite.

## 2. Results and Discussion

### 2.1. Characterization of the $g\text{-C}_3\text{N}_4\text{@Fe}_3\text{O}_4$ Composite

In this study, a sweat sensor was constructed with  $g\text{-C}_3\text{N}_4\text{@Fe}_3\text{O}_4$  intercalation structure materials (Figure 1) as sensitive primitives, with a subsequent application in the real-time monitoring of phosphoprotein. A nitrogen-doped  $g\text{-C}_3\text{N}_4$  was synthesized using melamine as raw material and urea as nitrogen source. It could effectively fill the nitrogen vacancy defect structure of  $g\text{-C}_3\text{N}_4$  formed by melamine and further improve the conductivity of  $g\text{-C}_3\text{N}_4$ . Figure S2a presents the morphology of melamine, which exhibited predominantly random particle shapes. Additionally, Figure S2b presents a heterogeneous layered structure of urea. The  $g\text{-C}_3\text{N}_4$  intermediate formed through the hydrothermal reaction of melamine and urea is shown in Figure S2c. Among them, melamine and urea further formed nanopillar clusters through the van der Waals stacking reaction. With the occurrence of hydrothermal reaction, the melamine molecule and the urea molecule underwent a self-assembly reaction, and the melamine was promoted to transform into a nano-columnar-like structure with a diameter of about 1.3  $\mu\text{m}$ . In addition, the interior of the nanocolumnars was continuously stacked by hydrogen bonds, which made the intermediates gradually pile up to form the aligned nanopillar-like cluster structure.

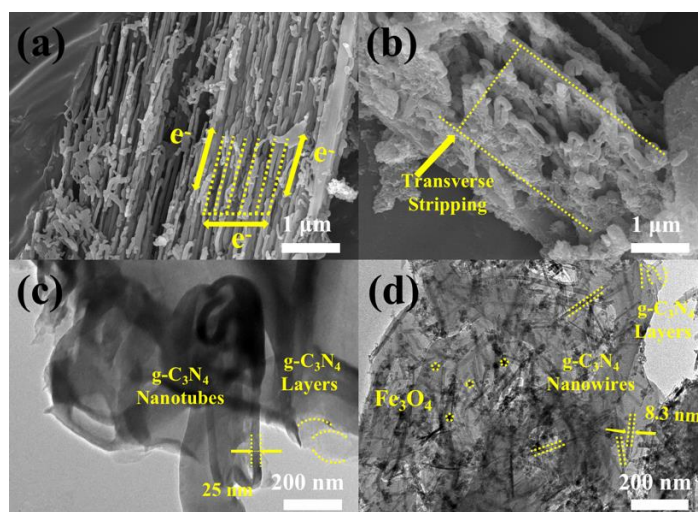


**Figure 1.** The  $g\text{-C}_3\text{N}_4$  SEM images of (a,b) at different viewing angles and TEM images of (c)  $g\text{-C}_3\text{N}_4$  and (d) CNFeO-0.4.

Figure 1a is a SEM image of the nitrogen-doped  $g\text{-C}_3\text{N}_4$  nanomaterials prepared by calcining the intermediate to form an intercalation structure. Interestingly, it can also be clearly observed from Figure 1b that  $g\text{-C}_3\text{N}_4$  showed sheet/tube/sheet structures. This is because the hydrogen bonds between the inner layers of the nanocolumnar cluster intermediates are destroyed by the gradual increase in temperature during the heating process of calcination. This further leads to transverse stripping of the intermediates to form isolated sheet/tube/sheet intercalated structures. In addition, these nanotube clusters were uniformly arranged on a coplanar surface, which could effectively improve the stability of the  $g\text{-C}_3\text{N}_4$  structure and facilitate the fast electron transport between nanotubes. The structure of  $g\text{-C}_3\text{N}_4$  nanomaterials was consistent with TEM observation. As shown in Figures 1c and S2g, with the prolongation of calcination time, the interior of the intermediate exfoliation layer gradually transformed into a nanotube cluster structure with a diameter of about 25 nm through self-rolling. Moreover, many curved nanotube clusters are arranged uniformly and orderly among the nanosheets. The preparation process of  $g\text{-C}_3\text{N}_4$  obviously underwent multi-step structural changes, in which the transverse stripping of the intermediates was the fundamental reason for reducing the diameter of  $g\text{-C}_3\text{N}_4$  tubes [27].

Then, the  $\text{Fe}_3\text{O}_4$  nanoparticles were in situ embedded on  $g\text{-C}_3\text{N}_4$  surfaces (Figure 1d) by co-precipitation with  $\text{FeSO}_4 \cdot 7\text{H}_2\text{O}$  and  $\text{FeCl}_3 \cdot 6\text{H}_2\text{O}$ , which have a specific adsorption capacity for phosphoproteins. The original intercalation structure of  $g\text{-C}_3\text{N}_4$  was still maintained. The reason considered was that after ultrasonic treatment, the weak bonds inside the  $g\text{-C}_3\text{N}_4$  were destroyed, so that many nanowire structures were formed on the basis of the original structure. The composite materials restrained each other while maintaining a uniform dispersion state, forming a heterojunction structure and effectively solving the agglomeration problem of nanoparticles. Overall, a point-line-plane trinity intercalation structure composite material structure was formed.

X-ray diffraction patterns in wide angle of the  $g\text{-C}_3\text{N}_4@Fe_3O_4$  composite (Figure 2a) displayed typical diffraction peaks of  $g\text{-C}_3\text{N}_4$  and  $Fe_3O_4$ , which could be indexed to JCPDS PDF#87-1526 and JCPDS PDF#99-0073. Specifically, the peaks at  $12.7^\circ$  and  $27.5^\circ$  were assignable to the diffractions of triazine unit structure stacking (100) and crystal and aromatic ring stacking (002) interlayer planes of  $g\text{-C}_3\text{N}_4$  [28,29]. Moreover, the powder diffraction data of  $Fe_3O_4$  particles include the characteristic peaks at  $30.1^\circ$ ,  $35.4^\circ$ ,  $43.1^\circ$ ,  $53.4^\circ$ ,  $56.9^\circ$ ,  $62.5^\circ$ , and, respectively, belonged to (220), (311), (400), (422), (511), (440) planes [30]. This showed that the introduction of different ratio of  $Fe_3O_4$  inhibits the superposition of  $g\text{-C}_3\text{N}_4$  in the vertical direction of the crystal plane, and there is no obvious peak shift.

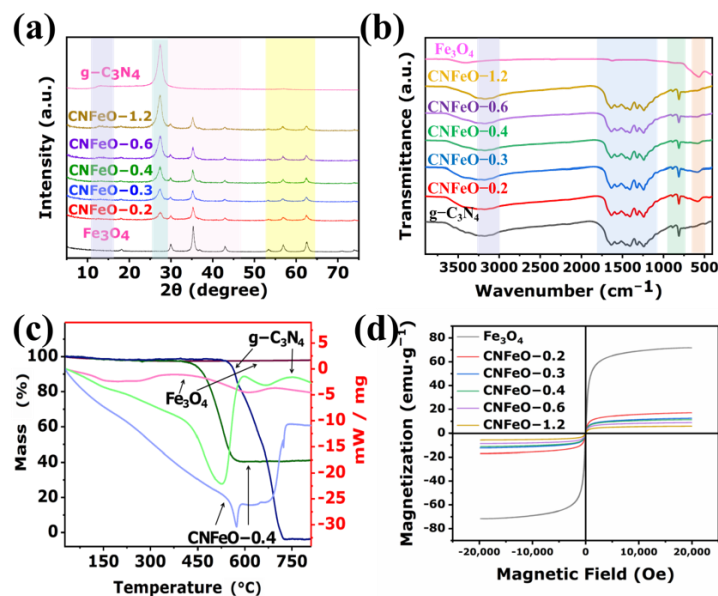


**Figure 2.** (a) XRD patterns and (b) FT-IR patterns of  $Fe_3O_4$ ,  $g\text{-C}_3\text{N}_4$ , and different ratio  $g\text{-C}_3\text{N}_4@Fe_3O_4$ , (c) TG/DSC patterns of  $Fe_3O_4$ ,  $g\text{-C}_3\text{N}_4$ , and  $CNFeO-0.4$ , (d) VSM patterns of  $Fe_3O_4$  and different ratio  $g\text{-C}_3\text{N}_4@Fe_3O_4$ .

FT-IR was performed as shown in Figure 2b. The absorption peak of  $g\text{-C}_3\text{N}_4$  at  $3186\text{ cm}^{-1}$  is caused by the N-H stretching vibration peak and the O-H vibration mode, where the surface absorbs moisture. The multiple absorption peaks located at  $1241\text{ cm}^{-1}$ ,  $1320\text{ cm}^{-1}$ ,  $1409\text{ cm}^{-1}$ ,  $1458\text{ cm}^{-1}$ ,  $1567\text{ cm}^{-1}$ ,  $1635\text{ cm}^{-1}$  correspond to the characteristic peaks of the aromatic C-N heterocyclic ring and stretching vibration. Additionally, the absorption peak at  $823\text{ cm}^{-1}$  belongs to the stretching vibration mode of the triazine ring structure molecule [31–33]. The absorption peak with a wavenumber of  $570\text{ cm}^{-1}$  is caused by the Fe-O vibration of pure  $Fe_3O_4$  [34]. Above all, the FT-IR spectra indicated the successful formation of the  $g\text{-C}_3\text{N}_4@Fe_3O_4$  composites.

The thermogravimetric analysis in Figure 2c explored the thermal stability of the material in an air atmosphere (Supplementary Materials, Section S3.2). The results showed that the thermal stability of the sensing materials could meet the standard of application at room temperature. The hysteresis regression line performance at room temperature is shown

in Figure 2d. The results showed that all nanomaterials are generally superparamagnetic (Supplementary Materials, Section S3.3).

XPS spectra of CNFeO-0.4 was performed as shown in Figure 3a. The peaks at 725.85 eV and 711.85 eV correspond to Fe2p<sub>1/2</sub> and Fe2p<sub>3/2</sub> of Fe<sub>3</sub>O<sub>4</sub>, respectively. Additionally, the peaks at 399.85 eV and 284.85 eV correspond to N1s and C1s of g-C<sub>3</sub>N<sub>4</sub>, respectively. Figure 3b shows the binding energy peaks at 284.8 eV, 286 eV, and 288.7 eV, corresponding to the C1s, which were, respectively, expressed as the surface-activated carbon C-C structure, C-N-C position bond structure, and sp<sup>2</sup> hybrid carbon C-(N)<sub>3</sub> structure [35–37]. Figure 3c shows the binding energy peaks at 399.1 eV, 400.5 eV, and 404.8 eV, corresponding to the N1s, which were, respectively, expressed as the tertiary amine pyrrole nitrogen N-(C)<sub>3</sub> structure, C-N-H structure, and π-excitation [38–40]. Figure 3d shows that the Fe2p peak could be disassembled into two strong characteristic peaks of Fe2p<sub>3/2</sub>, Fe2p<sub>1/2</sub> and two satellite peaks. The two photoelectron peaks of 711.65 eV and 724.9 eV are attributed to Fe<sup>3+</sup>, whereas 717.5 eV and 732.6 eV, respectively, correspond to two satellite peaks, further indicating the existence of Fe<sub>3</sub>O<sub>4</sub> [41,42]. Figure 3e shows the binding energy peaks at 529.5 eV, 530.5 eV, and 531.5 eV, corresponding to the O1s. It came from two different compounds in the sample linked to F-O, C-OH, and C-O-C structures [43–45]. These results prove the coexistence of g-C<sub>3</sub>N<sub>4</sub> and Fe<sub>3</sub>O<sub>4</sub> in the composite.

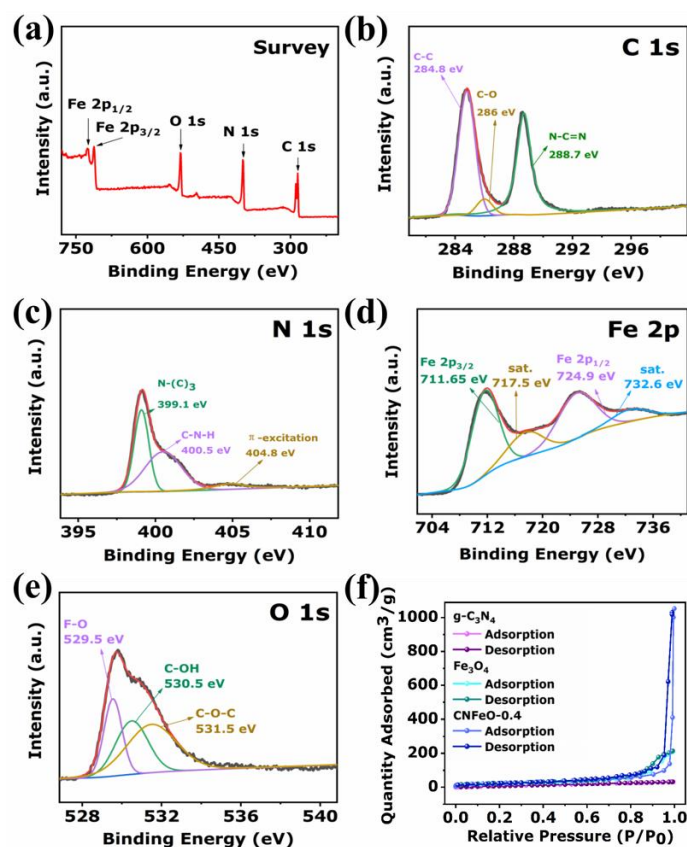


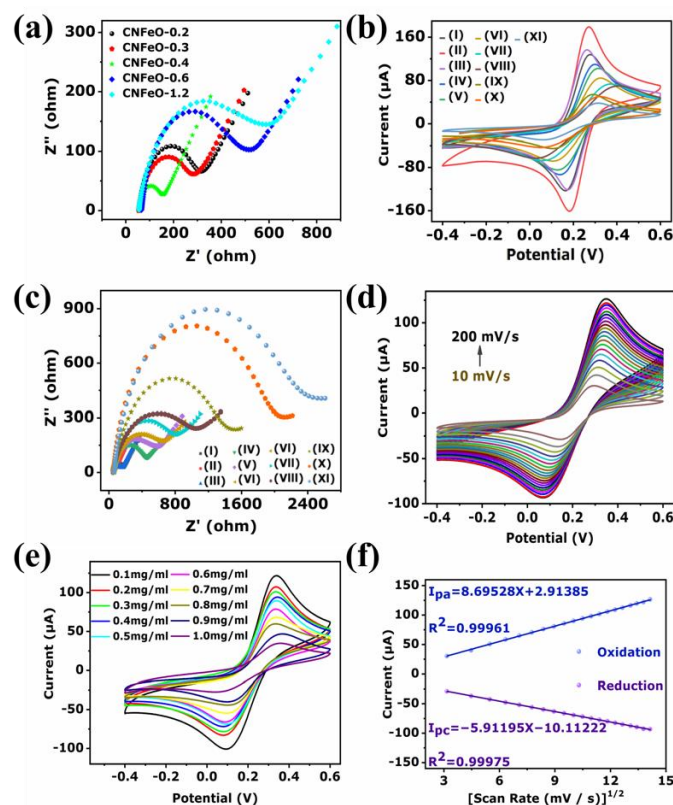
Figure 3. Full-scan XPS spectrum (a) and C 1s (b), N 1s (c), Fe 2p (d), and O 1s (e) of the g-C<sub>3</sub>N<sub>4</sub>@Fe<sub>3</sub>O<sub>4</sub>, and Nitrogen adsorption-desorption isotherms of (f) g-C<sub>3</sub>N<sub>4</sub>, Fe<sub>3</sub>O<sub>4</sub>, and CNFeO-0.4.

Figure 3f is the nitrogen adsorption-desorption isotherms of g-C<sub>3</sub>N<sub>4</sub>, Fe<sub>3</sub>O<sub>4</sub>, and g-C<sub>3</sub>N<sub>4</sub>@Fe<sub>3</sub>O<sub>4</sub>. The results show that the synthesized composite materials have a large specific surface area of 85.895 m<sup>2</sup>/g, which was significantly higher than that of g-C<sub>3</sub>N<sub>4</sub> (53.338 m<sup>2</sup>/g). It is caused by the presence of Fe<sub>3</sub>O<sub>4</sub> particles, which makes the exfoliation degree of the intercalation structure of g-C<sub>3</sub>N<sub>4</sub> more dispersed. Thus, the doping of Fe<sub>3</sub>O<sub>4</sub> could provide more active sites of g-C<sub>3</sub>N<sub>4</sub>, which was beneficial for improving the electron transport ability (Supplementary Materials, Figure S5). The results of Zeta potential show

that the isoelectric point of the  $g\text{-C}_3\text{N}_4\text{@Fe}_3\text{O}_4$  was  $\text{pH} = 5.747$ . (Supplementary Materials, Figure S4).

## 2.2. Phosphoprotein Sensing

The electron transfer ability of different  $g\text{-C}_3\text{N}_4\text{@Fe}_3\text{O}_4$  was analyzed by electrochemical impedance spectroscopy (EIS). As shown in Figure 4a, the CNFeO-0.4 possessed the best electron transfer ability. Therefore, CNFeO-0.4 was selected as the sensing material in the subsequent experiments. It can be seen from Figure S7a that the CV response of pure  $g\text{-C}_3\text{N}_4$  is significantly lower than that of  $g\text{-C}_3\text{N}_4$  doped with urea as the nitrogen source. Likewise, the EIS electron transfer ability of nitrogen-doped  $g\text{-C}_3\text{N}_4$ , as shown in Figure S7b, is significantly higher than that of pure  $g\text{-C}_3\text{N}_4$ .



**Figure 4.** (a) EIS of different proportions of  $g\text{-C}_3\text{N}_4\text{@Fe}_3\text{O}_4$ , (b) CV of electrodes under different modified conditions, (c) EIS of electrodes under different modified conditions, (d) CV under different sweep speeds of 10–200 mV/s, (e) CV for different concentrations of  $\beta$ -Casein (0.1 mg/mL to 1.0 mg/mL), and (f) Fitting equations and  $R^2$  for CV.

A pair of obvious redox peaks can be found in curve I (bare GCE) on the bare electrode, and the peak potential difference is about 110.0 V. The gold nanoparticles were modified on the surface of the bare electrode by electrochemical potentiostatic deposition, and the current intensity of curve II (Au/GCE) increased significantly to the largest current density. The reason is that the gold nanoparticles deposited by potentiostatic have excellent electrical conductivity, which promotes the rapid transfer of electrons [46,47].  $g\text{-C}_3\text{N}_4$  and  $\text{Fe}_3\text{O}_4$  are relatively unfavorable for the transfer of electric charges, leading to a decrease in the current values of curves IV ( $g\text{-C}_3\text{N}_4/\text{Au/GCE}$ ) and V ( $\text{Fe}_3\text{O}_4/\text{Au/GCE}$ ), respectively. The negative charge of  $g\text{-C}_3\text{N}_4$  would form a repulsion effect with cyanide ions, and the wide band gap (2.7 eV) of  $g\text{-C}_3\text{N}_4$  restricts and hinders electron transfer [48]. The relatively poor conductivity of  $\text{Fe}_3\text{O}_4$  leads to increased resistance to electron transfer in the redox process [49]. The current of curve III ( $g\text{-C}_3\text{N}_4\text{@Fe}_3\text{O}_4$ ) when forming a heterojunction was significantly higher than that of curves IV and V, respectively. This is because the  $g\text{-C}_3\text{N}_4\text{@Fe}_3\text{O}_4$  hetero-

junction can promote the transfer ability of electrons [50]. A strong Au-S covalent bond was formed on the active sites of gold on the electrode surface [51] after the dropwise addition of the MCH blocking solution (6-mercapto-1-hexanol). Thus, it could be observed that the current intensity of curve VI (MCH/g-C<sub>3</sub>N<sub>4</sub>@Fe<sub>3</sub>O<sub>4</sub>/Au/GCE), VII (MCH/g-C<sub>3</sub>N<sub>4</sub>/Au/GCE), and VIII (MCH/Fe<sub>3</sub>O<sub>4</sub>/Au/GCE) was significantly lower than that of curves III, IV, and V. Comparing the current intensity of curve IX (β-Casein/MCH/g-C<sub>3</sub>N<sub>4</sub>@Fe<sub>3</sub>O<sub>4</sub>/Au/GCE), X (β-Casein/MCH/g-C<sub>3</sub>N<sub>4</sub>/Au/GCE), and XI (β-Casein/MCH/Fe<sub>3</sub>O<sub>4</sub>/Au/GCE), it was found that the current intensity is further reduced. This is because β-Casein is a macromolecular protein, which hinders the effective area and active site of electron transfer in electrochemistry after specific adsorption [52]. In summary, it could be found that each step of the electrode modification process was relatively successful, and β-Casein was successfully adsorbed on the electrode surface.

Figures 4c and S7b are the EIS of electrode under different modification conditions. The charge transfer resistance (R<sub>ct</sub>) of curve I was about 118.0 Ω. The R<sub>ct</sub> of curve II was significantly reduced to approximately 14.5 Ω, which revealed that the gold nanoparticles promote the conductivity of the electrode. The R<sub>ct</sub> was significantly increased after the electrode was modified with g-C<sub>3</sub>N<sub>4</sub>@Fe<sub>3</sub>O<sub>4</sub>, g-C<sub>3</sub>N<sub>4</sub>, and Fe<sub>3</sub>O<sub>4</sub>, which were approximately 105.2 Ω, 417.7 Ω, and 532.2 Ω for curve III, IV, and V, respectively. The EIS of the constructed electrode further increased, since the R<sub>ct</sub> of curve VI, VII, and VIII were about 577.0 Ω, 764.57 Ω, and 992.4 Ω after the MCH was added to the seal. The R<sub>ct</sub> of curve IX, X, and XI were about 1463.1 Ω, 2055.9 Ω, and 2504.2 Ω, respectively. This was because the β-Casein hindered the transfer of electrons to a greater extent after the specific adsorption on the electrode surface.

The electrochemical reaction kinetics of β-Casein was examined on β-Casein/MCH/g-C<sub>3</sub>N<sub>4</sub>@Fe<sub>3</sub>O<sub>4</sub>/Au/GCE via CV with different scanned scan rates. In Figure 4d, both the oxidation peak currents (I<sub>pa</sub>) and reduction peak currents (I<sub>pc</sub>) increased with increasing scan rate from 10 to 200 mV/s. This phenomenon revealed the typical quasi-reversible electron transfer dynamics on the electrode [53]. The relationship between the response of the peak current change and the square root of the scan rate is shown in Figure S7c. The linear fit equations were expressed as I<sub>pa</sub> = 8.69528X + 2.91385 (R<sup>2</sup> = 0.99961) and I<sub>pc</sub> = -5.91195X - 10.11222 (R<sup>2</sup> = 0.99975), respectively. The fitting result means that the redox reaction of β-Casein at β-Casein/MCH/g-C<sub>3</sub>N<sub>4</sub>@Fe<sub>3</sub>O<sub>4</sub>/Au/GCE was an adsorption control process [54].

Figure 4e shows the CV response of MCH/g-C<sub>3</sub>N<sub>4</sub>@Fe<sub>3</sub>O<sub>4</sub>/Au/GCE with different concentrations of β-Casein. As the concentration of β-Casein increased, the oxidation peak and reduction peak currents were significantly reduced. The concentration increased from 0.1 mg/mL to 1 mg/mL, and the oxidation peak and reduction peak currents changed from 121.8 μA to 34.85 μA, and -100.9 μA to -27.53 μA, respectively. In Figure 4f, the linear fit equations were I<sub>pa</sub> = -90.92121X + 130.27267 (R<sup>2</sup> = 0.98551) and I<sub>pc</sub> = 71.85455X - 103.062 (R<sup>2</sup> = 0.96568), respectively. The R<sup>2</sup> of these fitting equations was close to 1, indicating that the obtained formulae were more accurate.

In Figure S7d, the correlation between different concentrations of β-Casein and the electrode current response was further determined by differential pulse voltammetry (DPV). It can be seen that, as the concentration of β-Casein increased from 0.1 mg/mL to 1 mg/mL, the peak current also decreased from 61.08 μA to 18.87 μA, which was consistent with the overall performance of the CV. The linear fit equation obtained in Figure S7e was Y = -44.5624X + 64.59933 (R<sup>2</sup> = 0.99221). The R<sup>2</sup> of the fitting equation was close to 1, indicating that the obtained formulae were more accurate. The limit of detection (LOD) was calculated by referring to Equation (1).

$$\sigma_{\text{LOD}} = \frac{3\text{SD}}{m} \quad (1)$$

where SD is the standard deviation value of the blank sample, and  $m$  is the slope value of the standard curve of the test substance. According to the calculation, the detection limit of the sensor is  $9.74 \mu\text{M}$ .

The electrochemical sensing performance of the  $\beta$ -Casein/MCH/g-C<sub>3</sub>N<sub>4</sub>@Fe<sub>3</sub>O<sub>4</sub>/Au/GCE was further compared with previously reported  $\beta$ -Casein sensors (Table S2). As shown, the  $\beta$ -Casein/MCH/g-C<sub>3</sub>N<sub>4</sub>@Fe<sub>3</sub>O<sub>4</sub>/Au/GCE had lower LOD. Furthermore, it is worth mentioning here that our work is the first to achieve the detection of phosphoproteins in sweat over a range of protein concentrations in sweat.

### 2.3. The Sensing Mechanism Analysis

From the above discussion on the structure and properties of g-C<sub>3</sub>N<sub>4</sub>@Fe<sub>3</sub>O<sub>4</sub>, in order to understand the interaction of the constructed composites and  $\beta$ -Casein, the density functional theory (DFT) was used to study the synergistic mechanism (Figure 5).

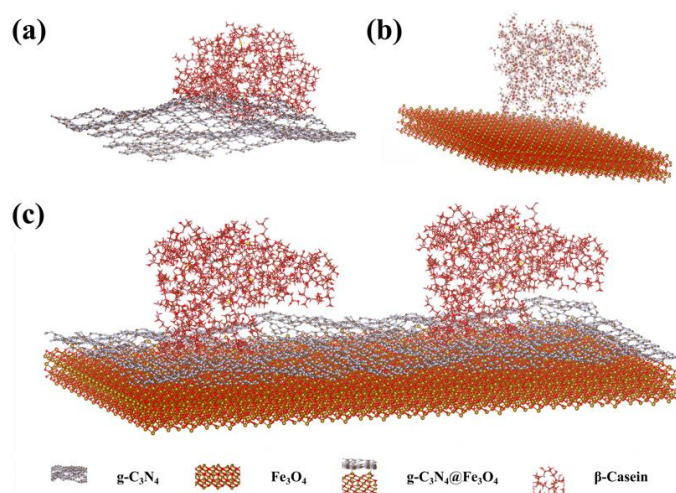


**Figure 5.** DFT coordination mechanism of (a) Fe<sub>3</sub>O<sub>4</sub>, (b) g-C<sub>3</sub>N<sub>4</sub> and (c) g-C<sub>3</sub>N<sub>4</sub>@Fe<sub>3</sub>O<sub>4</sub> on  $\beta$ -Casein, respectively.

Figure 5a represents the interaction of nitrogen-doped g-C<sub>3</sub>N<sub>4</sub> (gray-purple structural chain) and  $\beta$ -Casein, where red, crimson, brown, yellow, and purple balls represent O atom, H atom, C atom, S atom, and N atom. As shown in Figure 5a, a large number of H atoms in  $\beta$ -Casein closely adhere to N atoms in g-C<sub>3</sub>N<sub>4</sub> to form hydrogen bonds (N-H bonds). Here, the nitrogen-rich graphitic g-C<sub>3</sub>N<sub>4</sub> synthesized with urea doped with melamine possessed more N atoms on the g-C<sub>3</sub>N<sub>4</sub> surface, which effectively filled up many nitrogen vacancies formed on the surface of g-C<sub>3</sub>N<sub>4</sub> synthesized from pure melamine. The interaction between Fe<sub>3</sub>O<sub>4</sub> (gold-red chain structure) and  $\beta$ -Casein is shown in Figure 5b, in which the red and gold balls represent the O and Fe atoms, respectively. In Figure 5b, it is found that only the O atoms in  $\beta$ -Casein are adsorbed to the Fe atoms in Fe<sub>3</sub>O<sub>4</sub>. The Fe atoms would capture a large number of electrons from the O atoms to form Fe-O bonds, resulting in an increase in electronegativity of the O atoms, and the empty orbital could not form a hydrogen bond with the H atoms of the  $\beta$ -Casein. Therefore, the interaction effect is relatively weaker than that of g-C<sub>3</sub>N<sub>4</sub>. It can be found that the interaction between g-C<sub>3</sub>N<sub>4</sub> and  $\beta$ -Casein is better.

Figure 5c shows the interaction of g-C<sub>3</sub>N<sub>4</sub>@Fe<sub>3</sub>O<sub>4</sub> with  $\beta$ -Casein. The interaction was mainly through functional groups, such as N-C=N, N-(C)<sub>3</sub>, and C-N-H in g-C<sub>3</sub>N<sub>4</sub>@Fe<sub>3</sub>O<sub>4</sub> and the amino group (-NH<sub>2</sub>) of free amino acids in the shell of  $\beta$ -Casein protein to form N-H bonds. In addition, the larger specific surface area of the g-C<sub>3</sub>N<sub>4</sub>@Fe<sub>3</sub>O<sub>4</sub> composite also provided more active sites for the action of  $\beta$ -Casein. On the other hand, g-C<sub>3</sub>N<sub>4</sub> and Fe<sub>3</sub>O<sub>4</sub> could form a p-n-type heterostructure at the composite interface, which made the carriers have better spatial separation. It was conducive to the rapid transfer of electrons, and the overall synergy was presented. In addition, the electron transfer between g-C<sub>3</sub>N<sub>4</sub>@Fe<sub>3</sub>O<sub>4</sub> composite was through the Fe-N bonds. Structurally, there were many C-N bonds, C-C

bonds, C-H bonds, C-O bonds, O-H bonds, N-H bonds, and a small amount of C-S bonds in the  $\beta$ -Casein. In addition, there was a large number of C-N bonds and Fe-O bonds in  $g\text{-C}_3\text{N}_4$  and  $\text{Fe}_3\text{O}_4$ , respectively. The bond lengths of  $g\text{-C}_3\text{N}_4$ ,  $\text{Fe}_3\text{O}_4$  and  $g\text{-C}_3\text{N}_4@\text{Fe}_3\text{O}_4$  interacting with  $\beta$ -Casein are shown in Tables S3–S6, respectively. Additionally, the adsorption energy changes are shown in Table S7. As shown in Table S3, the bond length of  $g\text{-C}_3\text{N}_4@\text{Fe}_3\text{O}_4$  increased significantly after the interaction with  $\beta$ -Casein, which can be seen by comparing the bond length after the interaction of  $g\text{-C}_3\text{N}_4$ . In addition, the C-N bonds, Fe-O bonds in  $g\text{-C}_3\text{N}_4$  and  $\text{Fe}_3\text{O}_4$ , as well as the N-H bond lengths formed by  $g\text{-C}_3\text{N}_4$  and  $\beta$ -Casein were significantly increased (Tables S4–S6). This shows that the interaction between the composite and  $\beta$ -Casein was stronger, and the  $\beta$ -Casein was activated to a higher degree. It can also be seen from Figure 5c that  $g\text{-C}_3\text{N}_4@\text{Fe}_3\text{O}_4$  interacted with  $\beta$ -Casein, and the atoms in the  $g\text{-C}_3\text{N}_4$  structural chain were more closely arranged. More H atoms in the structure moved toward N atoms to form many N-H bonds. However,  $\text{Fe}_3\text{O}_4$  would transfer more electrons to  $g\text{-C}_3\text{N}_4$  through the Fe-N bonds formed in  $g\text{-C}_3\text{N}_4@\text{Fe}_3\text{O}_4$ , and the number of electrons in the N atomic energy band was higher. The result was that the N-H bonds formed with the H element in  $\beta$ -Casein were more stable, which enhanced the interaction effect of  $\beta$ -Casein to a greater extent.

In addition, the adsorption energies of all materials with  $\beta$ -Casein were negative, indicating that the adsorption process was exothermic. Therefore, the adsorption process was stable (Table S7).

#### 2.4. Selectivity, Reproducibility, and Stability

##### 2.4.1. Selectivity

The selectivity of the sensor toward  $\beta$ -Casein was evaluated in the presence of various common nonphosphoproteins (bovine serum albumin,  $\alpha$ -lactalbumin, and  $\beta$ -lactoglobulin) with the ratio of 1:100 ( $V_{\beta\text{-Casein}}:V_{\text{mixed nonphosphoproteins}}$ ). Figure 6a,b indicate that the  $g\text{-C}_3\text{N}_4@\text{Fe}_3\text{O}_4$  showed a significant response to  $\beta$ -Casein mixed with nonphosphoproteins but an inconspicuous response to these individual nonphosphoproteins. The results showed that the constructed phosphoprotein electrochemical sensor could selectively respond to phosphoprotein even under the complex system with different concentrations of nonphosphoprotein interference.

##### 2.4.2. Reproducibility

The reproducibility of  $g\text{-C}_3\text{N}_4@\text{Fe}_3\text{O}_4$  was performed in an electrolyte solution five times. The CV and current peak histogram results are shown in Figure 6c,d. The electrode-detected peak potentials were basically the same. The calculated relative standard deviation (RSD) of the measured results was 2.17%, which indicates that the constructed phosphoprotein electrochemical sensor has good reproducibility.

##### 2.4.3. Stability

The stability of the constructed sensor was tested by the same electrode with 10 mg/L  $\beta$ -Casein five consecutive times (Figure 6e,f). The RSD of the calculated peak current was 0.59%, which shows that the constructed phosphoprotein electrochemical sensor has good repeatability.

#### 2.5. Practical Application Sensor Evaluation

In order to verify the accuracy of this method, sweat monitoring in practical applications was performed by attaching a chip (Figure 7a). The specific device construction process is based on a PI flexible substrate chip with Au as the working electrode, Ag/AgCl as the reference electrode, and Pt as the counter electrode. It was further completed by spinning  $g\text{-C}_3\text{N}_4@\text{Fe}_3\text{O}_4$  sensing material and coating MCH blocking solution to block unreacted active sites and Tween-20 active agent solution. By constructing a  $g\text{-C}_3\text{N}_4@\text{Fe}_3\text{O}_4$  sensing array on a PI flexible three-electrode, the electrochemical chip was attached to the volunteer's curved arm without any separation (Figure 7b). An application of the CV

response of the sensor was obtained when a person cycled in a closed room for 15 min while drinking 100 mL milk, while the contrastive CV response was obtained from another person cycling for 15 min. The CV response of the former was significantly lower than that of the latter, as shown in Figure 7c. This was attributed to the macromolecular phosphoprotein metabolized from sweat adsorbed on the surface of  $g\text{-C}_3\text{N}_4\text{@Fe}_3\text{O}_4$ . These results indicate that the constructed phosphoprotein electrochemical sensor was potentially applicable for phosphoprotein in sweat in the real sample.

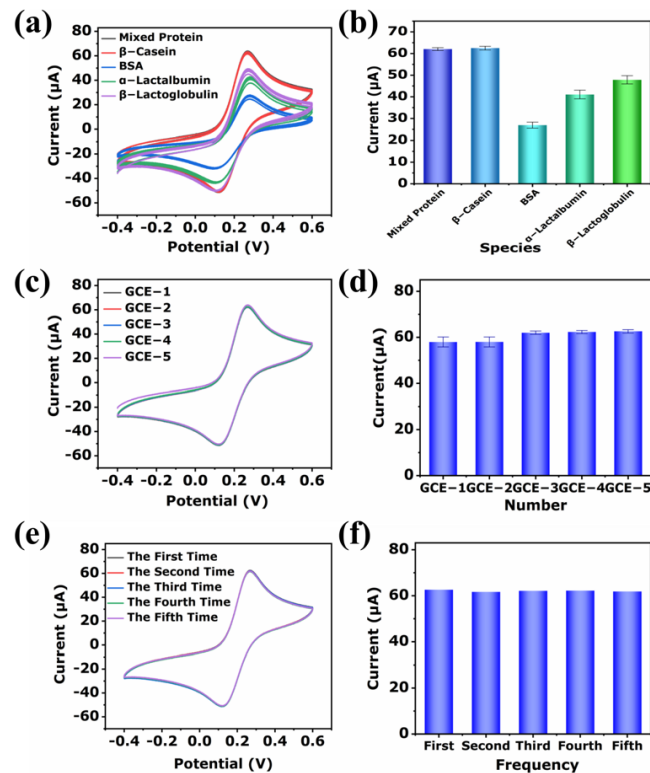


**Figure 6.** (a) CV of the selectivity of different protein adsorption electrodes to detect current and (b) selectivity histogram of CV, (c) CV of the stability of the detection current of five electrodes and (d) stability histogram of CV, (e) CV diagrams of the repeatability detected in parallel with one electrode and (f) repeatability histogram of CV.

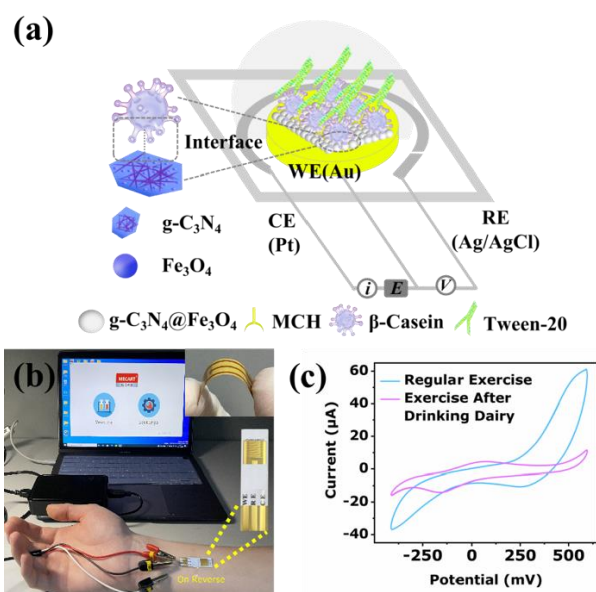


**Figure 7.** (a) Schematic diagram of wearable sweat sensor array, (b) Optical photo for real-time on-body sweat monitoring (Insert: Flexible sensing platform) and (c) Data-monitoring chart under different exercise conditions.

### 3. Conclusions

In conclusion, we developed a  $g\text{-C}_3\text{N}_4@Fe_3O_4$  intercalated composite as a specificity-sensitive moiety by hydrothermal synthesis, calcination, and co-precipitation. By constructing a sensing array on a flexible sensing platform, we demonstrated a skin-adhering, noninvasive, real-time, and in situ wearable sensing platform for sweat phosphoprotein monitoring. The detection limit of this electrochemical sensing platform could be as low as  $9.7 \mu\text{M}$ , and the detection range was  $10 \text{ mg/L}$  to  $1 \text{ mg/mL}$ . By combining the results of the adsorption between the intercalation structure  $g\text{-C}_3\text{N}_4@Fe_3O_4$  composite and the  $\beta\text{-Casein}$  with the density functional theory calculation, a better scientific rational explanation for the detection mechanism was provided. Thus, our sweat phosphoprotein monitoring wearable platform further enables applications in clinical monitoring and precision medicine. Combining spatial network big data and artificial intelligence technology, such as high-precision medical biosensors, could be further studied in real-time, noninvasive sweat monitoring and sweat metabolism phosphoproteomics.

**Supplementary Materials:** The following supporting information can be download at: <https://www.mdpi.com/article/10.3390/bios12060361/s1>, Figure S1: Sweatomics analysis; Figure S2: Morphology analysis; Figure S3: VSM patterns; Figure S4: Zeta potential; Figure S5: Pore diameter; Figure S6: Adsorption performance; Figure S7: Sensing performance; Table S1: MaxQuant parameters; Table S2: Related work comparsion; Tables S3–S7: DFT data; Table S8: Phosphoprotein table.

**Author Contributions:** Writing—original draft, Y.Q. and L.Q.; formal analysis, P.Z. (Peize Zhao); investigation, P.Z. (Peng Zhang), F.W. and J.Z.; writing—review and editing, L.G. and B.L.; visualization, L.Z. All authors have read and agreed to the published version of the manuscript.

**Funding:** This research was funded by the Natural Science Foundation of Qinghai Province, grant number 2020-ZJ-764 and Xining Science and Technology Bureau, grant number 2021-Y-08.

**Institutional Review Board Statement:** Not applicable.

**Informed Consent Statement:** Not applicable.

**Data Availability Statement:** Not applicable.

**Conflicts of Interest:** The authors declare no conflict of interest.

## References

1. Guan, W.; Shao, Z.; Shu, D.; Dong, L.; Lie, M.; Xia, P.; Hong, X.; Umar, F.; Wei, G.; Ji, L. Stretchable Optical Sensing Patch System Integrated Heart Rate, Pulse Oxygen Saturation and Sweat pH Detection. *IEEE Trans. Biomed. Eng.* **2019**, *66*, 1000–1005.
2. Mohan, V.; Rajendran, V.; Mishra, R.K.; Jayaraman, M. Recent Advances and Perspectives in Sweat based Wearable Electrochemical Sensors. *Trends Anal. Chem.* **2020**, *131*, 116024. [[CrossRef](#)]
3. Herrmann, W.P.; Habbig, J. Immunological studies on the proteins of human eccrine sweat. *Arch. Dermatol. Res.* **1976**, *255*, 123–127. [[CrossRef](#)] [[PubMed](#)]
4. Serag, A.; Shakkour, Z.; Halboup, A.M.; Kobeissy, F.; Farag, M.A. Sweat metabolome and proteome: Recent trends in analytical advances and potential biological functions. *J. Proteom.* **2021**, *246*, 104310. [[CrossRef](#)]
5. Tramutola, A.; Tramutol, A.; Lanzillotta, C.; Perluigi, M.; Butterfield, D.A. Oxidative stress, protein modification and Alzheimer disease. *Brain Res. Bull.* **2017**, *133*, 88–96. [[CrossRef](#)]
6. Engholm-Keller, K.; Martin, R.L. Technologies and challenges in large-scale phosphoproteomics. *Proteomics* **2013**, *13*, 910–931. [[CrossRef](#)]
7. Hwang, L.; Ayaz-Guner, S.; Gregorich, Z.R.; Cai, W.; Valeja, S.G.; Jin, S.; Ge, Y. Specific Enrichment of Phosphoproteins Using Functionalized Multivalent Nanoparticles. *J. Am. Chem. Soc.* **2015**, *137*, 2432–2435. [[CrossRef](#)]
8. Cohen, P. The role of protein phosphorylation in human health and disease. The Sir Hans Krebs Medal Lecture. *Eur. J. Biochem.* **2001**, *268*, 5001–5010. [[CrossRef](#)]
9. Hubbard, M.J.; Cohen, P. On target with a new mechanism for the regulation of protein phosphorylation. *Trends Biochem. Sci.* **1993**, *18*, 172–177. [[CrossRef](#)]
10. Lassen, P.S.; Thygesen, C.; Larsen, M.R.; Kempf, S.J. Understanding Alzheimer's disease by global quantification of protein phosphorylation and sialylated N-linked glycosylation profiles: A chance for new biomarkers in neuroproteomics? *J. Proteom.* **2017**, *161*, 11–25. [[CrossRef](#)]
11. Molinaro, L.; Hui, P.; Tan, M.; Mishra, R.K. Role of presynaptic phosphoprotein synapsin II in schizophrenia. *World J. Psychiatry* **2015**, *5*, 260–272. [[CrossRef](#)] [[PubMed](#)]
12. Martin, I. Ribosomal protein s15 phosphorylation mediates LRRK2 neurodegeneration in Parkinson's disease. *Cell* **2014**, *157*, 472–485. [[CrossRef](#)] [[PubMed](#)]
13. Ashman, K.; Villar, E.L. Phosphoproteomics and cancer research. *Clin. Transl. Oncol.* **2009**, *11*, 356–362. [[CrossRef](#)] [[PubMed](#)]
14. Kotlo, K.; Johnson, K.R.; Grillon, J.M.; Geenen, J.M.; Tombe, P.; Danziger, R.S. Phosphoprotein abundance changes in hypertensive cardiac remodeling. *J. Proteom.* **2012**, *77*, 1–13. [[CrossRef](#)]
15. Reddy, M.M.; Quinton, P.M. CAMP-independent phosphorylation activation of CFTR by G proteins in native human sweat duct. *Am. J. Physiol. Cell Physiol.* **2001**, *280*, 604–613. [[CrossRef](#)]
16. Reddy, M.M.; Quinton, P.M. ENaC Activity Requires CFTR Channel Function Independently of Phosphorylation in Sweat Duct. *J. Membr. Biol.* **2005**, *207*, 23–33. [[CrossRef](#)]
17. Murota, H.; Matsui, S.; Ono, E.; Kijima, A.; Kikuta, J.; Ishii, M.; Katayama, I. Sweat, the driving force behind normal skin: An emerging perspective on functional biology and regulatory mechanisms. *J. Dermatol. Sci.* **2015**, *77*, 3–10. [[CrossRef](#)]
18. Reddy, M.M.; Quinton, P.M. PKA Mediates Constitutive Activation of CFTR in Human Sweat Duct. *J. Membr. Biol.* **2009**, *231*, 65–78. [[CrossRef](#)]
19. Shi, G.; Sun, Z.; Liu, M.; Zhang, L.; Liu, Y.; Qu, Y.; Jin, L. Electrochemistry and Electrocatalytic Properties of Hemoglobin in Layer-by-Layer Films of SiO<sub>2</sub> with Vapor—Surface Sol—Gel Deposition. *Anal. Chem.* **2007**, *79*, 3581–3588. [[CrossRef](#)]
20. Li, Q.; Luo, G.; Feng, J. Direct Electron Transfer for Heme Proteins Assembled on Nanocrystalline TiO<sub>2</sub> Film. *Electroanalysis* **2001**, *13*, 359–363. [[CrossRef](#)]
21. Yao, Z.; Jin, Y.; Yun, D.; Bo, L. Research progress on g-C<sub>3</sub>N<sub>4</sub>-based photocatalysts for organic pollutants degradation in wastewater: From exciton and carrier perspectives. *Ceram. Int.* **2021**, *172*, 682–711.
22. Gong, Y.; Li, M.; Li, H.; Wang, Y. Graphitic carbon nitride polymers: Promising catalysts or catalyst supports for heterogeneous oxidation and hydrogenation. *Green Chem.* **2015**, *17*, 715–736. [[CrossRef](#)]
23. Min, C.; Li, R.; Li, Y.; Qin, J.; Yang, X. In-Situ fabrication of Ag/g-C<sub>3</sub>N<sub>4</sub> composite materials with improved photocatalytic activity by coordination-driven assembly of precursors. *Ceram. Int.* **2016**, *42*, 5575–5581. [[CrossRef](#)]
24. Lei, L.; Qiang, H.; Wu, L.; Xi, X.; Peng, L.; Dong, S.; Xin, W.; Xu, Y. Well-Combined Magnetically Separable Hybrid Cobalt Ferrite/Nitrogen-Doped Graphene as Efficient Catalyst with Superior Performance for Oxygen Reduction Reaction. *Small* **2016**, *11*, 5833–5843.
25. Reddy, L.H.; Arias, J.L.; Nicolas, J.; Couvreur, P. Magnetic nanoparticles: Design and characterization, toxicity and biocompatibility, pharmaceutical and biomedical applications. *Chem. Rev.* **2012**, *112*, 5818–5878. [[CrossRef](#)] [[PubMed](#)]
26. Wang, B.; Wu, H.; Yan, Y.; Tang, K.; Ding, C. In Situ synthesis of a novel metal oxide affinity chromatography affinity probe for the selective enrichment of low-abundance phosphopeptides. *Rapid Commun. Mass Spectrom.* **2020**, *34*, e881. [[CrossRef](#)] [[PubMed](#)]
27. Jiang, G.; Wang, X.; Zhu, A.; Gong, J.; Liu, F.; Wang, Y.; Zhao, C. Cl/S co-doped carbon nitride nanotube clusters effectively drive the metal-free photo-Fenton reaction under visible light: A new ROS conversion mechanism. *Carbon* **2022**, *190*, 32–46. [[CrossRef](#)]
28. Lotfi, Z.; Gholivand, M.B.; Shamsipur, M. Introduction of a non-enzymatic glucose sensor based on a g-C<sub>3</sub>N<sub>4</sub>/NiO/CuO nanocomposite. *Anal. Biochem.* **2020**, *616*, 114062. [[CrossRef](#)]

29. Li, J.; Cao, C.; Zhu, H. Synthesis and characterization of graphite-like carbon nitride nanobelts and nanotubes. *Nanotechnology* **2007**, *18*, 11. [[CrossRef](#)]
30. Bi, L.; Wen, S.; Wen, Z.; Xiao, Z.; Shun, P.; Hai, W.; Yong, S.; Yan, X. Fe<sub>3</sub>O<sub>4</sub>@CNT as a high-effective and steady chainmail catalyst for tetracycline degradation with peroxydisulfate activation: Performance and mechanism. *Sep. Purif. Technol.* **2021**, *173*, 118705.
31. Wang, M.; Cui, S.; Yang, X.; Bi, W. Synthesis of g-C<sub>3</sub>N<sub>4</sub>/Fe<sub>3</sub>O<sub>4</sub> nanocomposites and application as a new sorbent for solid phase extraction of polycyclic aromatic hydrocarbons in water samples. *Talanta* **2015**, *132*, 922–928. [[CrossRef](#)] [[PubMed](#)]
32. Imran, H.; Manikandan, N.; Dharuman, V. Highly selective and rapid non-enzymatic glucose sensing at ultrathin layered Nb doped C<sub>3</sub>N<sub>4</sub> for extended linearity range. *Microchem. J.* **2020**, *160*, 105774. [[CrossRef](#)]
33. Li, C.; Xu, J.; Zhang, Y.; Cheng, Z.; Lei, W.; Hao, Q. g-C<sub>3</sub>N<sub>4</sub> nanofibers doped poly(3,4-ethylenedioxythiophene) modified electrode for simultaneous determination of ascorbic acid and acetaminophen. *J. Electroanal. Chem.* **2018**, *824*, 52–59. [[CrossRef](#)]
34. Zheng, H.; Ding, J.; Zheng, S.; Zhu, G.; Feng, Y. Facile synthesis of magnetic carbon nitride nanosheets and its application in magnetic solid phase extraction for polycyclic aromatic hydrocarbons in edible oil samples. *Talanta* **2016**, *148*, 46–53. [[CrossRef](#)] [[PubMed](#)]
35. Wang, Y.; Wang, Y.; Zhu, Y. Nanoporous graphitic carbon nitride with enhanced photocatalytic performance. *Catal. Commun.* **2013**, *29*, 10566–10572.
36. Xiang, Q.; Zhang, J.; Jaroniec, M. Preparation and Enhanced Visible-Light Photocatalytic H<sub>2</sub>-Production Activity of Graphene/C<sub>3</sub>N<sub>4</sub> Composites. *J. Phys. Chem. C* **2011**, *115*, 8915–8923. [[CrossRef](#)]
37. Jie, Y.; Fang, C.; Yu, S.; Jun, G.; Xian, L. Assembled porous Fe<sub>3</sub>O<sub>4</sub>@g-C<sub>3</sub>N<sub>4</sub> hybrid nanocomposites with multiple interface polarization for stable microwave absorption. *Ceram. Int.* **2018**, *44*, 19207–19216.
38. Kailasam, K.; Schmidt, J.; Bildirir, H.; Gui, Z.; Blechert, S.; Xin, W.; Thomas, A. Room Temperature Synthesis of Heptazine-Based Microporous Polymer Networks as Photocatalysts for Hydrogen Evolution. *Macromol. Rapid Commun.* **2013**, *34*, 1008–1013. [[CrossRef](#)]
39. Zeng, Y.; Liu, C.; Wang, L.; Zhang, S.; Ding, Y.; Xu, Y.; Liu, Y.; Luo, S. A three-dimensional graphitic carbon nitride belt network for enhanced visible light photocatalytic hydrogen evolution. *J. Mater. Chem. A* **2016**, *4*, 19003–19010. [[CrossRef](#)]
40. Dan, Z.; Lu, P.; Ke, L.; Hermenegildo, G.; Chuan, S. Cobalt nanoparticle with tunable size supported on nitrogen-deficient graphitic carbon nitride for efficient visible light driven H<sub>2</sub> evolution reaction. *Chem. Eng. J.* **2020**, *381*, 122576.
41. Mousavi, M.; Habibi-Yangjeh, A.; Seifzadeh, D. Novel ternary g-C<sub>3</sub>N<sub>4</sub>/Fe<sub>3</sub>O<sub>4</sub>/MnWO<sub>4</sub> nanocomposites: Synthesis, characterization, and visible-light photocatalytic performance for environmental purposes. *J. Mater. Sci. Technol.* **2018**, *34*, 1638–1651. [[CrossRef](#)]
42. Jin, C.; Yun, Q.; Wang, M.; Jie, H.; Rong, G. Aqueous Solution-Based Fe<sub>3</sub>O<sub>4</sub> Seed-Mediated Route to Hydrophilic Fe<sub>3</sub>O<sub>4</sub>-Au Janus Nanoparticles. *Langmuir* **2016**, *32*, 4595–4601. [[CrossRef](#)] [[PubMed](#)]
43. Ramalingam, T.; Anandaram, S. Spectroscopic and DFT investigations on the corrosion inhibition behavior of tris (5-methyl-2-thioxo-1,3,4-thiadiazole) borate on high carbon steel and aluminium in HCl media. *RSC Adv.* **2013**, *3*, 23681–23691.
44. Stoch, J.; Gablankowskakgukucz, J. The effect of carbonate contaminations on the XPS O 1s band structure in metal oxides. *Surf. Interface Anal.* **2010**, *17*, 165–167. [[CrossRef](#)]
45. Karakeçili, A.G.; Demirtas, T.T.; Satriano, C.; Gümüşderelioglu, M.; Marletta, G. Evaluation of L929 fibroblast attachment and proliferation on Arg-Gly-Asp-Ser (RGDS)-immobilized chitosan in serum-containing/serum-free cultures. *J. Biosci. Bioeng.* **2007**, *104*, 69–77. [[CrossRef](#)] [[PubMed](#)]
46. Ali, B.; Afsaneh, D.; Mohammad, M.; Fatemeh, M.; Reza, Z. Electrochemical deposition of gold nanoparticles on reduced graphene oxide modified glassy carbon electrode for simultaneous determination of levodopa, uric acid and folic acid. *J. Electroanal. Chem.* **2015**, *736*, 22–29.
47. Jin, W.; Bei, Y.; Hui, W.; Ping, Y.; Yu, D. Highly sensitive electrochemical determination of Sunset Yellow based on gold nanoparticles/graphene electrode. *Anal. Chim. Acta* **2015**, *893*, 41–48.
48. Hatamie, A.; Jalilian, P.; Rezvani, E.; Kakavand, A.; Simchi, A. Fast and ultra-sensitive voltammetric detection of lead ions by two-dimensional graphitic carbon nitride (g-C<sub>3</sub>N<sub>4</sub>) nanolayers as glassy carbon electrode modifier. *Measurement* **2019**, *134*, 679–687. [[CrossRef](#)]
49. Ning, K.; Li, J.; Jun, Z.; Xian, Z.; Xian, W.; Hui, L.; Xin, Z.; Feng, Y. Uniform growth of Fe<sub>3</sub>O<sub>4</sub> nanocubes on the single-walled carbon nanotubes as an electrosensor of organic dyes and the study on its catalytic mechanism. *J. Electroanal. Chem.* **2019**, *833*, 70–78.
50. Chinnapaiyan, S.; Chen, T.; Chen, S.; Alothman, Z.; Chang, W. Ultrasonic-assisted Preparation and Characterization of Magnetic ZnFe<sub>2</sub>O<sub>4</sub>/g-C<sub>3</sub>N<sub>4</sub> Nanomaterial and their Applications towards Electrocatalytic Reduction of 4-Nitrophenol. *Ultrason. Sonochem.* **2020**, *68*, 105071. [[CrossRef](#)]
51. Kokkin, L.; Ruo, Z.; Steimle, T.; Wyse, I.; Pearlman, W.; Varberg, D. Au-S Bonding Revealed from the Characterization of Diatomic Gold Sulfide, AuS. *J. Phys. Chem. A* **2015**, *119*, 11659–11667. [[CrossRef](#)] [[PubMed](#)]
52. Cao, Q.; Zhao, H.; Yang, Y.; He, Y.; Nan, D.; Jian, W.; Wu, Z.; Xiang, K.; Wang, G. Electrochemical immunosensor for casein based on gold nanoparticles and poly(L-Arginine)/multi-walled carbon nanotubes composite film functionalized interface. *Biosens. Bioelectron.* **2011**, *26*, 3469–3474. [[CrossRef](#)] [[PubMed](#)]

- 
53. Yang, B.; Chun, L.; Ting, C.; Wen, L.; Sha, Z.; Ye, P.; Yong, L.; Huan, P. MXene-Copper/Cobalt Hybrids via Lewis Acidic Molten Salts Etching for High Performance Symmetric Supercapacitors. *Angew. Chem.* **2021**, *60*, 25318–25322.
  54. Shu, C.; Jing, X.; Min, S.; Yong, Y.; Quan, X.; Xue, D.; Yan, G.; Li, L. Polydopamine bridged MXene and NH<sub>2</sub>-MWCNTs nanohybrid for high-performance electrochemical sensing of Acetaminophen. *Appl. Surf. Sci.* **2021**, *570*, 151149.